Accepted Manuscript

Title: Pilot Investigation of Feedback Electronic Image Generation in Electron Beam Melting and its Potential for In-Process Monitoring

Authors: Hay Wong, Derek Neary, Sohail Shahzad, Eric Jones, Peter Fox, Chris Sutcliffe

PII: S0924-0136(18)30452-7
DOI: https://doi.org/10.1016/j.jmatprotec.2018.10.016
Reference: PROTEC 15969

To appear in: *Journal of Materials Processing Technology*

Received date: 5-1-2018
Revised date: 9-9-2018
Accepted date: 14-10-2018

Please cite this article as: Wong H, Neary D, Shahzad S, Jones E, Fox P, Sutcliffe C, Pilot Investigation of Feedback Electronic Image Generation in Electron Beam Melting and its Potential for In-Process Monitoring, *Journal of Materials Processing Tech.* (2018), https://doi.org/10.1016/j.jmatprotec.2018.10.016

Pilot Investigation of Feedback Electronic Image Generation in Electron Beam Melting and its Potential for In-Process Monitoring

Authors: Hay Wong[a], Derek Neary[a], Sohail Shahzad[a], Eric Jones[b], Peter Fox[a], Chris Sutcliffe[a]

[a]School of Engineering, University of Liverpool, The Quadrangle, Brownlow Hill, United Kingdom L69 3GH

[b]Jones Consultancy, Ardlahan, Kildimo, Co. Limerick, Ireland

Corresponding author's email: Hay Wong – hay.wong@liv.ac.uk

Keywords: Additive Manufacturing; Electron Beam Melting; Metallic Materials; In-Process Monitoring; Quality Control; Electronic Imaging; Secondary Electrons; Backscattered Electrons

##COLOR SHOULD BE USED FOR ALL FIGURES IN PRINT##

Abstract

Electron Beam Melting (EBM) is an additive manufacturing technique increasingly used by many industrial sectors, including the medical and aerospace industries. The application of this technology is, however, challenged by the lack of process monitoring and control systems to monitor process repeatability and component quality reproducibility. Various monitoring systems, mainly involving thermal and optical cameras, have been employed in previous attempts to study the quality of the EBM process. However, these systems have

limitations, which include: (1) images generated unavoidably include monitoring-irrelevant regions beyond the processing area and (2) images are subject to keystone distortion. In this paper, a digital electronic imaging system prototype is described for the Arcam A1 EBM machine. This paper aims to: (1) disseminate the prototype design, (2) demonstrate the prototype ability to overcome limitations of the existing thermal and optical imaging systems, (3) showcase the potential for the prototype to serve as an alternative EBM monitoring technique, and (4) serve as a pilot study for future in-process EBM monitoring research with electronic imaging. Digital electronic images were generated by detecting both secondary electrons and backscattered electrons originating from interactions between the machine electron beam and the processing area using specially designed hardware. Prototype capability experiments at room temperature and approximately $320°C$ were conducted with digital images being generated and analysed from a Ti-6-Al-4V (as demonstrator material) test build. Results suggest that this prototype has significant potential to be used for in-process monitoring of EBM in many manufacturing sectors.

Introduction

Electron Beam Melting (EBM) is an Additive Manufacturing (AM) technique that makes use of an accelerated electron beam to melt metallic powder on a layer-by-layer basis, forming components based on the geometries of the imported three dimensional Computer Aided Design (CAD) models, as explained by **Gibson et al. (2010)**. The ability of the EBM process to form components from metallic powder arises from electron interactions with metallic materials. When an electron beam is accelerated by an anode, focused onto a powder bed by an electromagnetic focusing coil and subsequently deflected to specific locations by an electromagnetic deflection coil, the electrons penetrate the powder grains, whereupon they slow down and convert their kinetic energy into thermal energy. If the energy input is sufficient, the temperature of the powder particles rises above their melting point and solid-

to-liquid phase transformation is initiated i.e. the particle melts. When the beam is raster-scanned across the preheated powder bed in a tightly controlled, predefined pattern, melt tracks are solidified to form fully dense cross sections of the desired components. This process is repeated with additional requirement that the underlying solid is also partially melting to ensure adequate bonding between the underlying and newly formed layers ensuring that full density achieved.

It is believed that the technique has great potential in the manufacture of components with complex designs and structures. In an evaluation study on powder based EBM technology, **Gong et al. (2014)** concluded that the EBM process would have the capability to enable the manufacture of a wide range of difficult to fabricate aerospace and biomedical components. **Harrysson et al. (2007)** and **Baudana et al. (2016)** investigated the mechanical properties of titanium implants and microstructures of test specimens built by the EBM process respectively. **Harrysson et al. (2007)** indicated that the increased design freedom of the EBM process enables the economic manufacture of porous bone ingrowth surfaces for orthopedic implants while **Baudana et al. (2016)** demonstrated that the reduced thermal residual stress and the high vacuum process environment would be beneficial for the production of aircraft components. Nevertheless, both of these industrial sectors are highly regulated and their current standard manufacturing processes used in them are well established, as identified by **Jarow et al. (2015)** and **Portolés et al. (2016)**. Their studies on regulations and qualification procedures used concluded that despite the perceived benefits of the EBM process, transition from the current standard manufacturing techniques to a layered manufacturing approach would not be possible unless a rigorous EBM process monitoring and validation system is available. **Mani et al. (2015)** shared the same concern in their report on the needs for real time control of additive manufacturing powder bed fusion processes.

Academic research groups have made efforts building different monitoring systems to assess the quality of the EBM process. For open-loop systems, a high speed optical camera was used by **Scharowsky et al. (2012)** to assess the melt pool size. There have been many attempts involving the use of Infrared (IR) thermal cameras. For example, **Price et al. (2012)** set up a near IR thermal camera to monitor preheating, contour melting and hatching events, while **Dinwiddie et al. (2013)** and **Schwerdtfeger et al. (2012)** employed IR cameras to detect porosity and flaws. Efforts have also been made to develop close loop feedback control systems. **Rodriguez et al. (2012)** demonstrated how to modify build settings by capturing and analyzing the surface temperature of the build chamber while **Mireles et al. (2015)** showed how to apply feedback to manipulate grain size in Ti-6Al-4V microstructures. Both **Rodriguez et al. (2012)** and **Mireles et al. (2015)** were using IR cameras.

The monitoring systems referenced focused on the use of thermal and optical imaging. There are however, issues when carrying out monitoring with these systems. Firstly, the cameras are mounted on top of the machine chamber and monitoring of the processing area is carried out through a viewing window. Field of View (FOV) of images captured by these systems may include monitoring-irrelevant regions beyond the processing area. Secondly, depending on the camera location, an orthogonal projection of the processing area cannot be guaranteed, and images with non-orthogonal projections would be distorted due to keystone effect. **Fig. 1 (a)** shows the location of the state-of-the-art near-IR camera which comes with the Arcam A1 EBM machine, hereafter referred to as the EBM machine, as a standard kit. The machine electron gun occupies the location directly above the processing area, thus the near-IR camera can only be mounted on an off-centred location, viewing the processing area at an angle. **Fig. 1 (b)** is a screenshot taken from the machine computer, showing an image captured by the near-IR camera. The figure demonstrates the described

imaging issues on FOV and keystone effect. It is thought that these two issues would hinder effective monitoring of the EBM process.

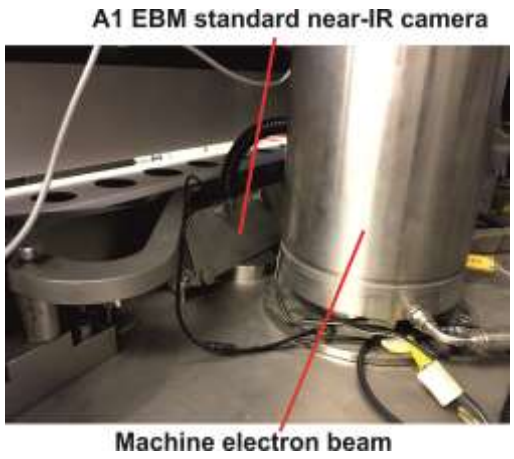

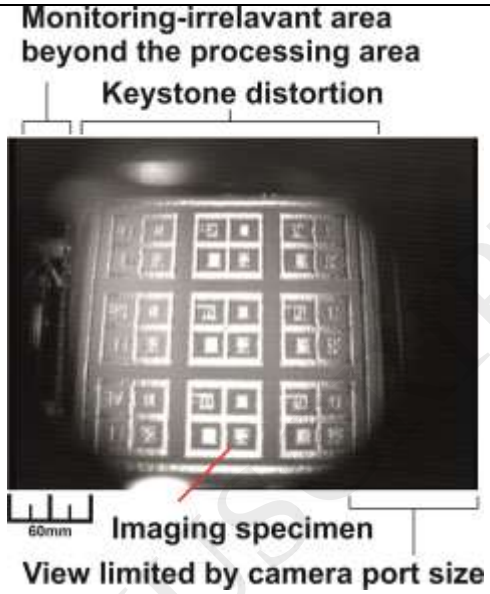

(a) (b)

Fig. 1. (a) The Arcam A1 EBM machine electron gun and its off-centred, state-of-the-art near-IR camera. (b) EBM machine computer screenshot of an image taken from the near-IR camera at room temperature, on a Ti-6Al-4V test build

It is believed that electronic imaging, which employs similar principles to those used in a Scanning Electron Microscope (SEM), offers an alternative to the existing EBM process monitoring techniques. Due to its image generation mechanism, the electronic image is inherently immune to the above mentioned issues faced by thermal and optical cameras. Writing on the principles of electron microscopy, **Watt (1997)** noted that in a typical analogue SEM, when a focused, accelerated primary electron beam is raster-scanned across a conductive target surface with the use of electromagnetic lens, Secondary Electrons (SE) and Backscattered Electrons (BSE) are generated from interactions between the primary electron beam and the conductive target. **Reimer (1998)** pointed out that some of the primary electrons may undergo elastic scattering with the target atoms and scatter back as BSE.

During scattering, a portion of energy from either the primary electrons or the BSE may be transferred to the atomic electrons in the conduction band of the target atoms via inelastic scattering. With sufficient energy, such energized atomic electrons may escape from the atoms. If these electrons are close enough to the target surface, they may successfully avoid being re-absorbed and be emitted as SE. In an analogue SEM, the SE and BSE, hereafter collectively referred to as feedback electrons, are first captured by an electron sensor, turned into electrical signal, undergo amplification and subsequently used to generate an analogue fluorescent image on a cathode-ray tube. The generation of feedback electrons is sensitive to the topographical characteristics of the conductive target. In an early account on the SEM instrumentation, **Oatley (1972)** noted that the change in composition, texture or topography at the point where the primary electrons strike the target, would consequently cause variations in the feedback electron signal acquired and thus give rise to image contrast on the cathode-ray tube. Upon reviewing the advantages presented by digital SEM, **Postek et al. (1996)** commented, in comparison to analogue SEM, that instead of projecting an image onto a phosphor screen in a cathode-ray tube, digital SEM stores and generates an image digitally with the use of electronics. In addition, variations in the feedback electron signal level manifest themselves as different grayscale pixel values in a digital image.

Given the ability of electronic imaging to reveal the topography of a conductive area, it is believed that the incorporation of an electronic imaging system in the EBM process will offer an alternative to the existing camera based monitoring techniques.

Materials and Methods

Bespoke electron sensors, signal processing electronics and image generation software were developed to build a EBM process monitoring system prototype. Preliminary testing and image capabilty verficiation of the prototype were carried out. The prototype was

then interfaced with the EBM machine, for the generation of digital electronic images during single-layer monitoring scans at room and elevated temperature. The specification of these systems is described below.

Electron Sensor Design

The EBM machine makes use of a heat shield, which comprises a stainless steel frame and a set of stainless steel plates. The heat shield is an important part of the EBM process as it contains the heat and captures condensed material within the machine processing area. As feedback electrons bombard the heat-shield during the EBM process, it was postulated that the electronically conductive heat shield could be modified to serve as an electron sensor.

To enable the heatshield to be used as an electron sensor it first had to be electronically insulated from the rest of the machine. This was enabled by the introduction of ceramic spacing components to separate and thereby insulate the heat shield from the machine chamber. Ceramics were selected because of their high melting temperature and low thermal and electrical conductivities. In addition, a set of stainless steel plates, which were used as noise capturing surfaces, were also electrically insulated from both the machine chamber and the heat shield by the use of ceramics. **Fig. 2 (a)** and **(b)** show the heat shield modifications. To sum up, the key design elements of the electron sensor are: (1) the sensor must contain electronically conductive surfaces to capture the feedback electrons, (2) the sensor must be electronically insulated from the rest of the machine, and (3) the sensor surfaces must surround the entire immediate vicinity of the processing area to guarantee good signal level. The geometry and/or design of the sensor presented in **Fig. 2 (a)** and **(b)** is merely one of many possible embodiments, thus its exact design details are of no critical importance to readers who would like to fabricate a similar electron sensor.

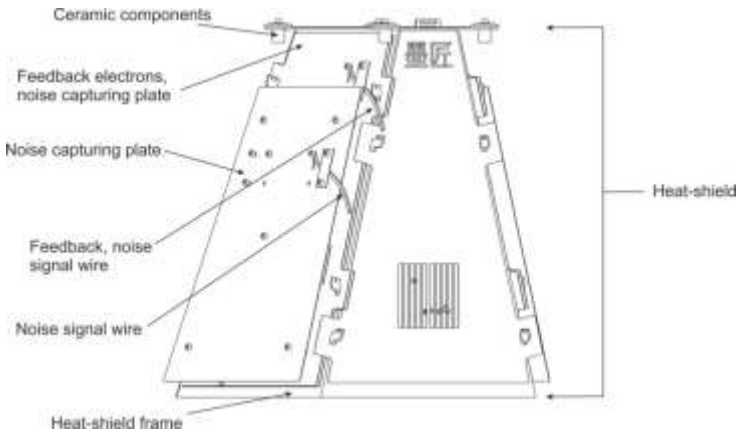

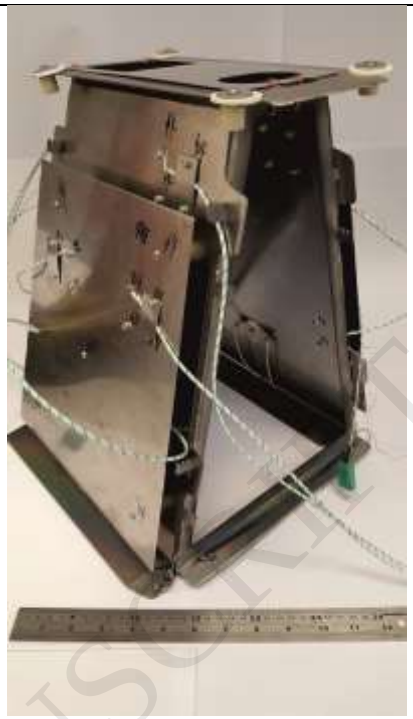

(a) (b)

Fig. 2. (a) Design of the electron sensor and (b) the electron sensor prototype

Signal Processing Electronics Design

The signal processing electronics consisted of a differential signal amplifier and a data logger. As illustrated in **Fig.3**, output of the amplifier, which is the feedback signal with enhanced Signal-to-Noise Ratio (SNR), is fed to the data logger for further processing. Data acquired by the data logger was temporarily stored in its built in memory and transmitted via Universal Serial Bus (USB) to a monitoring computer. **Fig. 4** describes the data logger process flow.

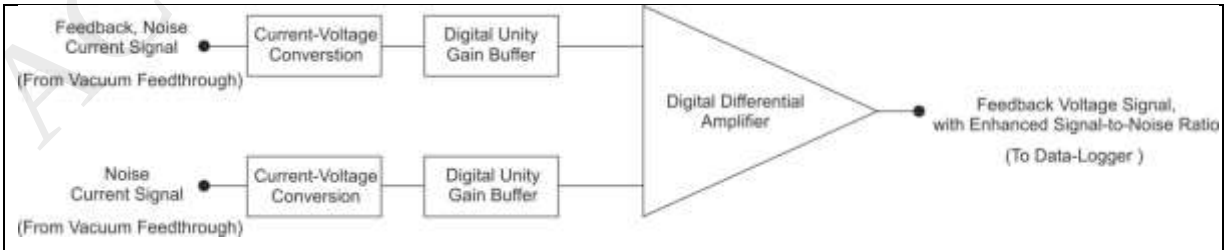

Fig.3. Block diagram of the differential signal amplifier

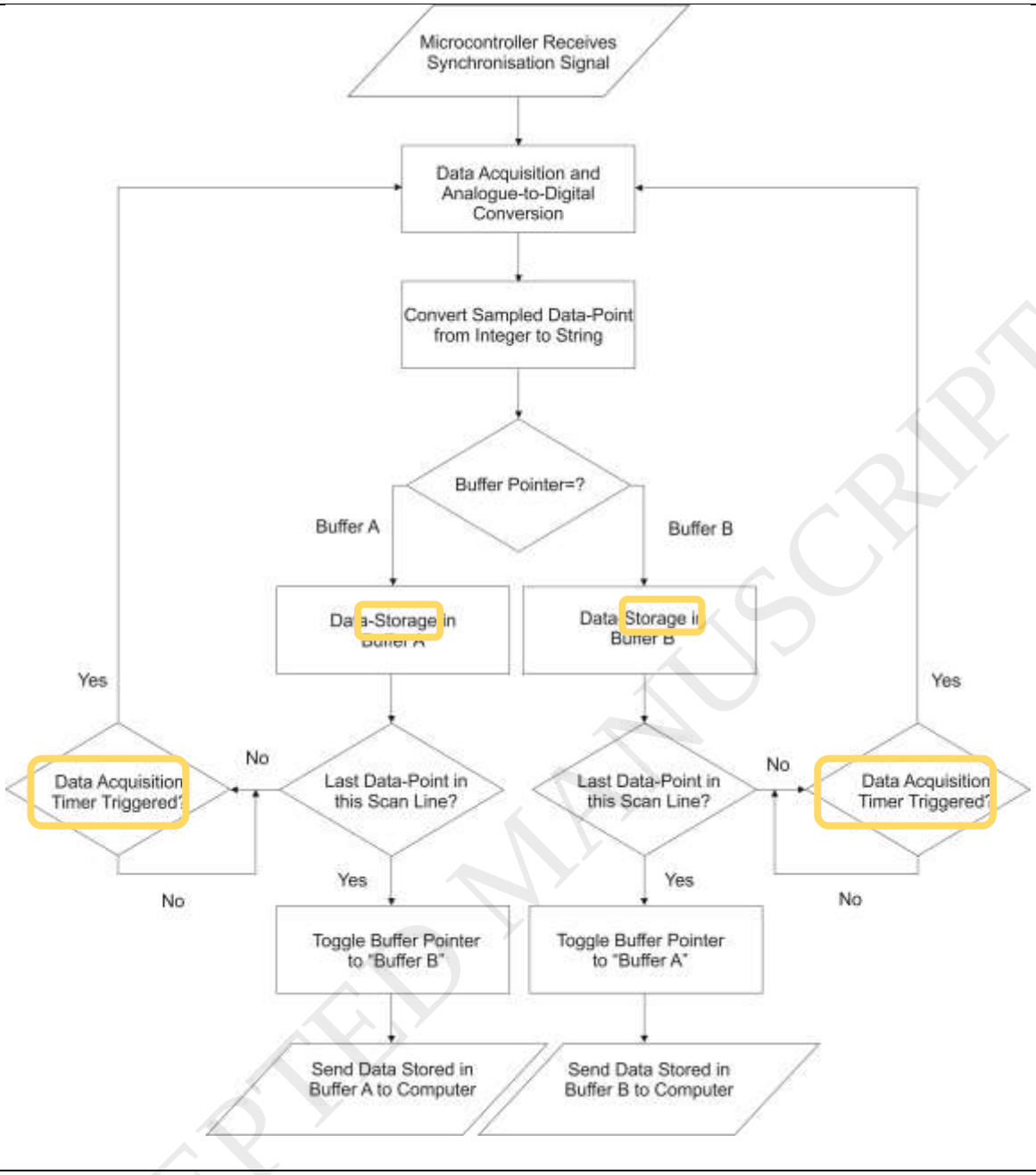

Fig. 4. Data logger process flow chart

Fig. 4 shows that the data acquisition cycle was initiated by a synchronisation signal, the function of which was to pick up the start of every scan line when the primary electron beam was conducting a raster-scanning pattern. This signal was designed to ensure that data-acquisition was synchronised with movement of the primary electron beam during melting. To activate the data acquisition function, the EBM machine beam X and Y scan signals,

which were used as location commands for the machine electromagnetic deflection coil, were fed into the data logger. **Fig. 5 (a)** gives an example of the typical machine X and Y scan signals during raster-scanning and **5 (b)** shows the corresponding raster-scanning pattern.

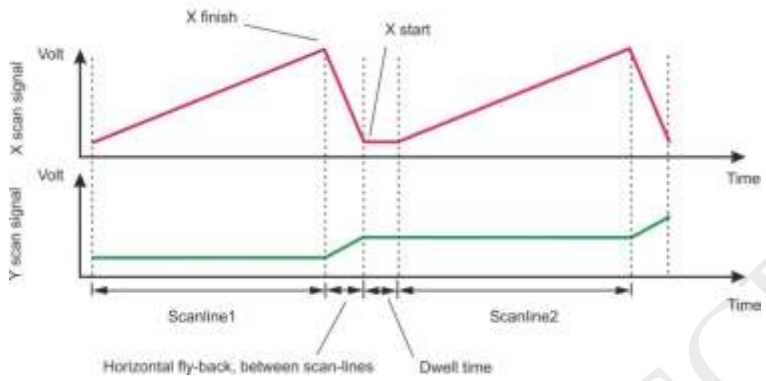

(a)

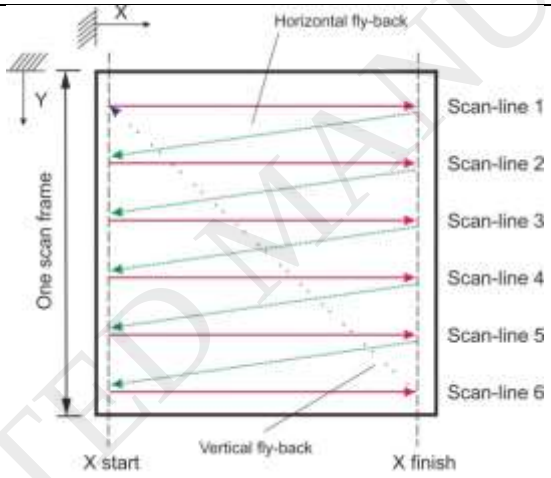

(b)

Fig.5. (a) Typical raster-scanning signals in a two dimension Cartesian plane, the X scan signal is a sawtooth waveform, directing the electron beam to move from left to right while the Y signal uses step increments to deflect the beam onto a new scan line. (b) The resultant raster-scanning pattern consists of multiple scan lines

Preliminary Feedback Electron Signal Detection Test

A preliminary test was set up to explore if the electron sensor and the differential signal amplifier could detect and process any feedback electron signals from the EBM machine during a single-layer monitoring scan at room temperature. The monitoring area consisted of a $200mm \times 50mm \times 1mm$ $(W \times D \times H)$ aluminium plate resting on top of a $200mm \times 200mm \times 1mm$ $(W \times D \times H)$ stainless steel plate. In the test, the primary electron beam raster-scanned an area of $200mm \times 200mm$, from top left to bottom right covering both plates, while the sensor and electronics captured and processed the data. In SEM imaging, BSE signal shows material contrast due to differences in atomic number (Egerton, 2005). As the sensor was designed to capture both SE and BSE, it was expected that there would be a contrast in the feedback electron signal level between aluminium and stainless steel. **Fig. 6 (a)** and **(b)** show the preliminary test setup and results respectively.

(a)

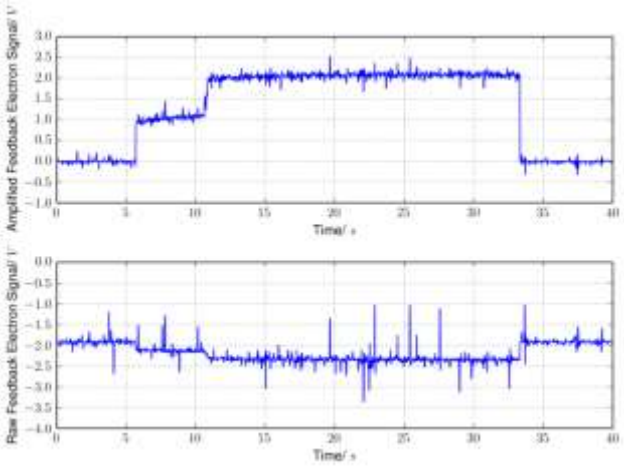

(b)

Fig. 6. (a) Preliminary test setup with an aluminium plate resting on top of a stainless steel plate. (b) Test results from oscilloscope showing signal contrast between aluminium and stainless steel

Both raw and amplified feedback electron signals in **Fig. 6 (b)** illustrate that signals are registered during the monitoring scan, between approximately $5s$ to $33s$ a. In addition, differences in signal level are observed between the signal originated from aluminium and that from stainless steel. The former gives rise to an amplified signal at approximately $1V$, sampled between about $5s$ to $10s$ whilst the latter at approximately $2V$, sampled between about $10s$ to $33s$. Qualitatively speaking, the amplified signal shows a greater SNR when compared with the raw signal. The results demonstrate that feedback electron signals generated from the EBM machine during monitoring scans at room temperature can be captured and processed by the electron senor and differential signal amplifier. The sensor and amplifier capabilities have been verified.

Image Generation Software Design

Following the acquisition of feedback electron signal by the electron sensor, data processed by the signal processing electronics (signal amplifier and data logger) was

designed to be transmitted to the monitoring computer for the generation of digital images. **Fig. 7** describes the image generation software process flow.

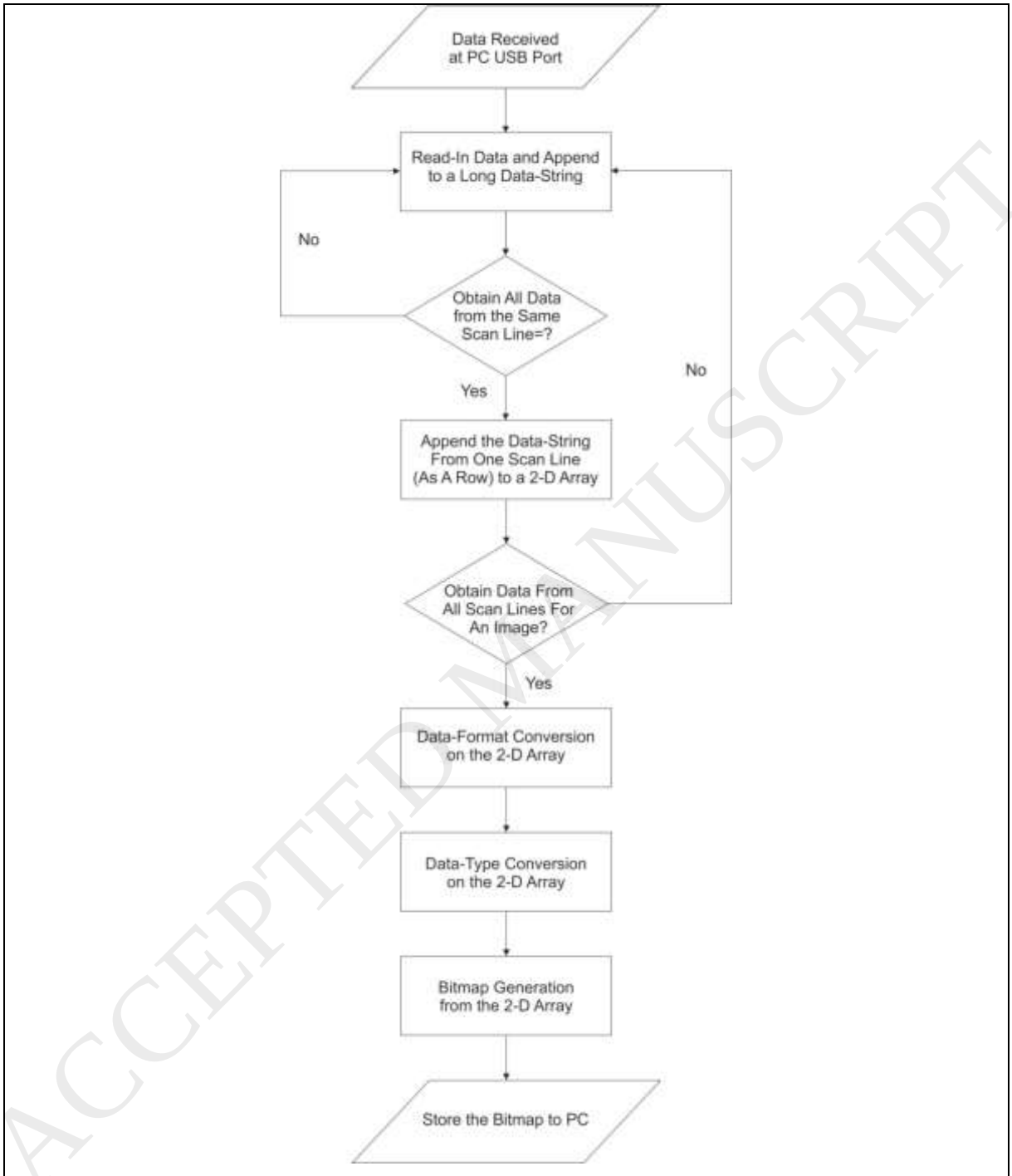

Fig. 7. Image generation software process flow chart

The software was designed to allow various input parameters such as, image size in pixel, image bit depth, file name and image format to be user-defined. Imported data from the data logger was sliced accordingly and converted to individual data point of integer

values. For the generation of a digital image, the individual data points were then allocated to their corresponding rows and columns to form a greyscale bitmap.

Experimental Setup

The electron sensor, signal processing electronics and the image generation software together formed an electronic imaging system prototype for the EBM process. Three sets of digital image generation experiments were conducted. The first set aimed to verify the prototype data acquisition and image generation ability while the second and third verified the prototype ability to generate electronic images when interfaced with the EBM machine.

In the first set of experiment, a benchtop test was conducted at room temperature to verify the data acquisition and image generation abilities of the prototype. Unlike signal collection by the electron sensor inside the EBM machine, data acquisition and image generation are conducted outside the machine, at room temperature, under real-life condition. In the test, a virtual machine X scan signal and a virtual feedback electron signal in voltage were generated by a specially developed waveform generator which simulated the electronic imaging process. The virtual signals were fed into the prototype for the generation of digital images. **Fig. 8** gives the block diagram of the waveform generator and **Fig. 9 (a)** and **(b)** give the waveform generation configuration for the test.

Fig. 8.Block diagram of the waveform generator

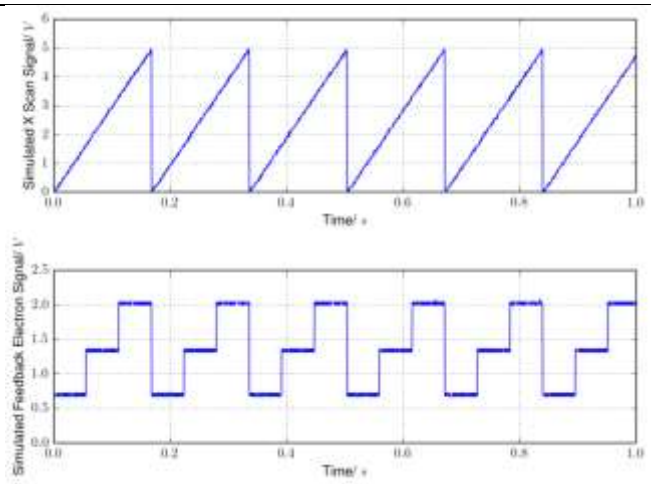

(a)

(b)

Fig.9. (a) A fraction of the virtual machine X scan and virtual feedback electron signals simulated by the waveform generator, in order to simulate a (b) $800\,pixel \times 2000\,pixel\,(row \times column)$ digital image with three equally-spaced stripes

The two virtual signals shown in **Fig. 9 (a)**, simulate an electronic imaging process with a raster-scanning pattern. The virtual X scan signal was in a sawtooth waveform to simulate the primary electron beam horizontal movement while the virtual feedback electron signal was assigned to have three voltage levels to represent an image with three equally spaced stripes with different pixel values in grayscale, as shown in **Fig. 9 (b).** Using this system prototype, capability could be verified by the successful waveform reconstruction of the three-stripe image prior to any active experimentation on the EBM machine. **Table. 1** gives the benchtop test settings in virtual signal simulations and waveform reconstruction.

Table. 1. Benchtop test settings

Benchtop Test Parameter	Value
Virtual feedback electron signal levels	$0.67V, 1.33V, 2.00V$
Data logger sampling frequency	$132kHz$
Data logger input/output range	$0\ to + 3.3V$
Image size ($row\ \times column$)	$800\ pixel\ \times\ 2000\ pixel$
Image bit depth	$8 - bit, 256$

In the second set of experiment, the prototype was interfaced with the EBM machine to investigate into image generation from the machine chamber. Single-layer electronic imaging trials were carried out on a Ti-6Al-4V (as a demonstrator material due to its popularity in the field of additive manufacturing as pointed out by **Dutta (2017)**) test build at room temperature. The test build was manufactured by EBM, from Ti-6Al-4V powder of $45\mu m - 106\mu m$ in size. **Fig. 10 (a)** and **(b)** depict the design of the test build and **Fig.11** is the schematic of the experimental setup.

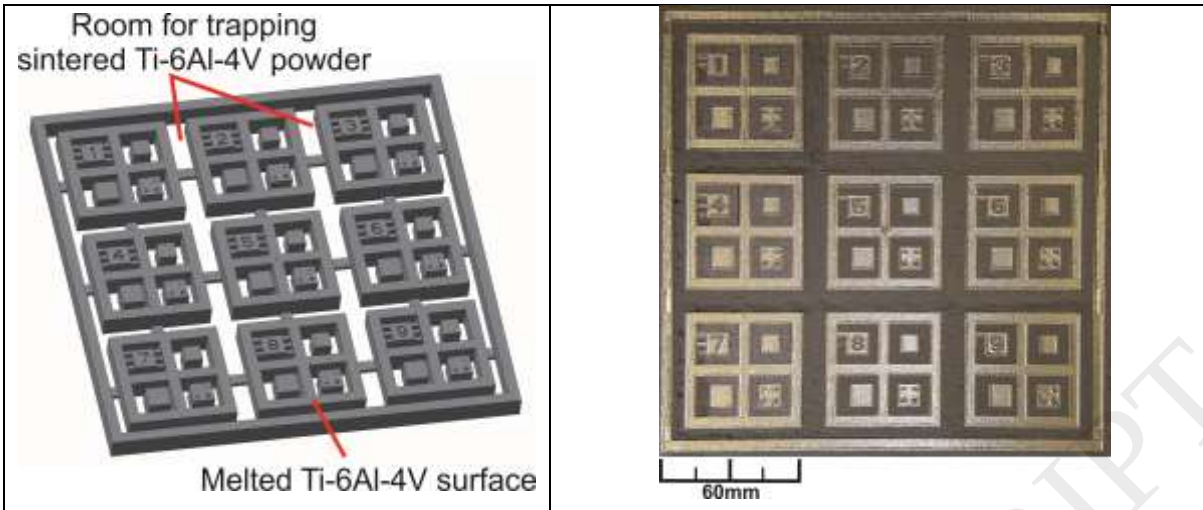

(a) (b)

Fig. 10. (a) CAD design of the standard electronic imaging test build. The room between the nine frames was designed to hold sintered powder during an EBM build. (b) The completed test build manufactured by the EBM machine with Ti-6Al-4V powder

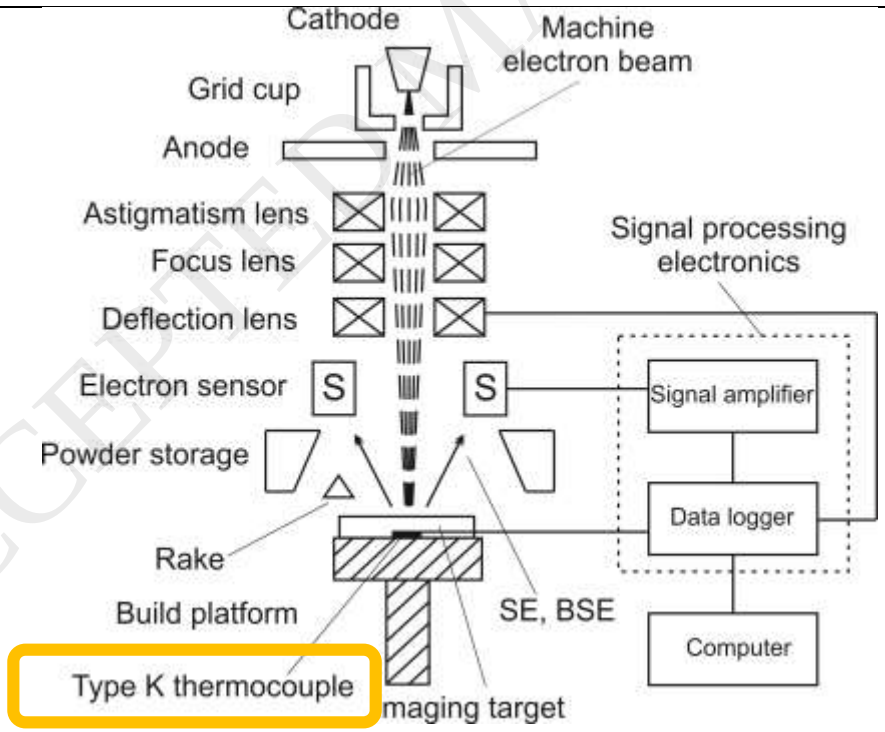

Fig. 11. Schematic of the electronic imaging trials setup

The test build shown in **Fig. 10 (a)** was developed as a standard electronic imaging test build. It was designed for investigating the image contrast in pixel value between sintered powder and solidified surfaces.

In the third set of experiment, the imaging trails carried out in the second set were repeated at elevated temperature. In a typical EBM build, the processing area is maintained at an elevated temperature by electron beam heating. For example, in any Ti-6Al-4V EBM builds, this preheating temperature is approximately at $700°C$ (Kirchner et al, 2014). In the experiment, a type K thermocouple placed underneath the Ti-6Al-4V test build was used to measure temperature and the machine electron beam heated up the test build via an in-house developed heating raster-scanning strategy, in the same manner as in electronic imaging depicted by **Fig. 5(b)**. The current experimental setup could only heat up the test build to approximately $320°C$ due to the rate of heat loss to the machine chamber. **Table. 2** and **3** outline the configurations of the prototype and EBM machine in the second and third set of experiments.

Table. 2. Electronic imaging system prototype configuration

Prototype Parameter	Value
Differential signal amplifier gain	10
Data logger sampling frequency	$118.8kHz$
Data logger input/output range	$0V - +3.3V$
Image size ($row \times column$)	$1800\ pixel \times 1800\ pixel$
Image bit depth	$8 - bit, 256$

Table. 3. EBM machine configuration

Machine Parameter	Value
Imaging area $(W \times D)$	$180mm \times 180mm$
Imaging temperature	$25°C / 320°C$
Chamber vacuum level	10^{-3}mbar
Beam current	$1mA\ (imaging) / 48mA\ (heating)$
Beam speed	$11880\ mms^{-1}(imaging) / 35000mms^{-1}(heating)$
Beam focus offset	$0\ mA\ (imaging) / 80mA\ (heating)$

Results

This section presents the results on system prototype capability verification and digital electronic image generation at both room and elevated temperatures.

System Capability Verification

The benchtop test was conducted to verify the digital image generation capability of the prototype. The simulated three-stripe image was reconstructed. **Fig. 12 (a)** and **(b)** below present the typical reconstruction results.

(a)

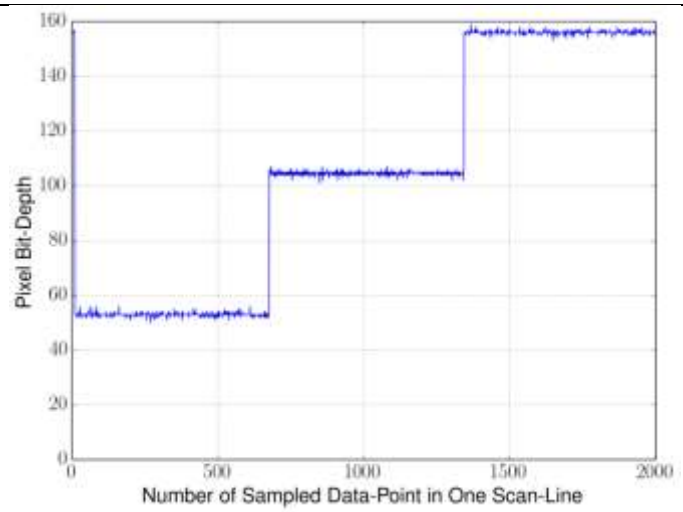

(b)

Fig. 12. Waveform reconstruction results: (a) a typical reconstructed three-stripe image of 800 $pixel$ × 2000 $pixel$ (row × $column$) in size and the (b) pixel values (sampled virtual feedback electron signal) plot of a typical waveform from a data set of 30 waveforms

Images with three stripes of different pixel values were generated. The average pixel value of a stripe in the reconstructed grayscale image was defined by **Eq. 1**.

$$L_i = \frac{V_{DL_i}}{V_{DL_{MAX}}} \times A \tag{1}$$

Where:

L_i – average pixel value. $i = 1, 2, 3$, representing the three stripes

V_{DLi} – average sampled pixel voltage (from feedback electron) received at the data logger. $i = 1, 2, 3$, representing the three voltages of the three-stripe region

V_{DLMAX} – maximum input voltage of the data logger, which is $+3.3V$ for the test

A – grayscale bit depth of an image, $A = 256$, 8-bit, in the case of the benchtop test

A successful reconstructed image from the benchtop test consisted of 2000 pixels in a pixel row, i.e. one waveform. A total of 30 waveforms, 60,000 data points of the sampled virtual feedback electron signal data point were randomly chosen from the result data set to analyse the accuracy of the signal level and data acquisition cycle of the data logger. The mean (μ), standard deviation (σ) and coefficient of variation, (C_V) of the pixel values and the number of pixel allocated for the representation of each of the three-stripe regions in the reconstructed image were calculated. **Table. 4** and **5** show the results of the analyses.

Table. 4. Average pixel values of the three-stripe region. Data are rounded to 3.s.f.

Parameter	Theoretical Pixel Value	μ	σ	C_V (%)
L_1	52.0	53.2	1.42	2.67
L_2	103	105	1.10	1.04
L_3	155	156	0.72	0.46

Table. 5. Average number of pixels in each section of the three-stripe region. Data are rounded to 3.s.f.

Section in a Scan Line	Theoretical Number of Pixel	μ	σ	C_V (%)
Stripe 1	667	666	0.00	0.00
Stripe 2	667	668	0.00	0.00
Stripe 3	666	666	0.00	0.00

Result from **Table. 4** shows that the variations in pixel value within each of the three-stripe region give rise to a C_V value of less than 3% and the μ of pixel values in the three-stripe region obtained are all less than 2% different from their theoretical values. Result from

Table. 5 shows that there are no variations in the number of pixels allocated in each of the three-stripe regions for the 30 waveforms analysed and the μ of number of pixels in each section of a scan line are less than 1% different from their theoretical vales.

Digital Image Generation at Room Temperature

The prototype was interfaced with the EBM machine and single-layer electronic imaging trials were carried out under room temperature. Various subsystem electrical signals were monitored and recorded during the imaging trials to aide trouble shooting. **Fig. 13 (a)** depicts the $180mm \times 180mm$ $(W \times D)$ imaging area and **Fig. 13 (b) – (c)** give the typical subsystem signals.

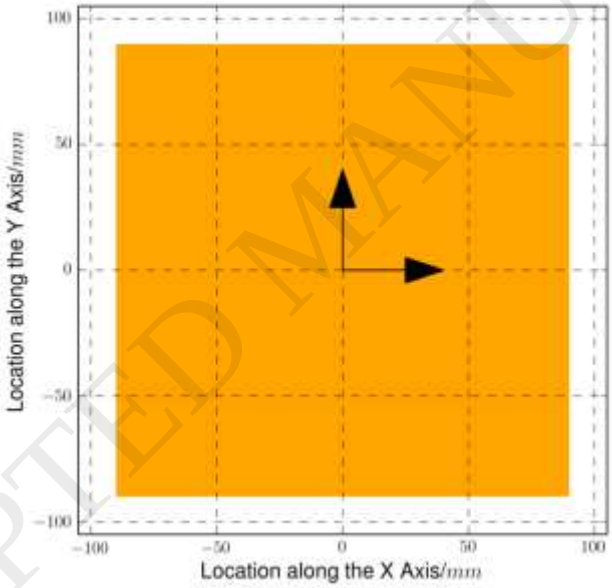

(a)

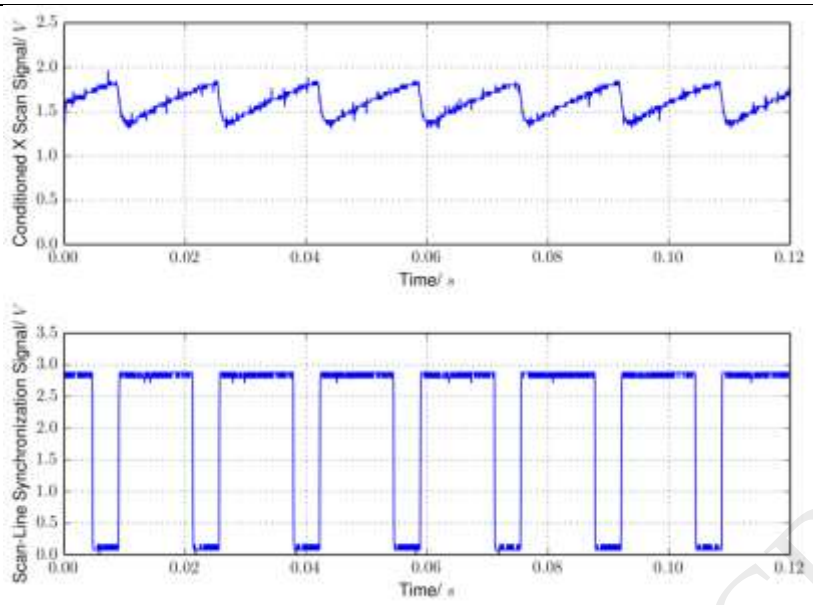

(b)

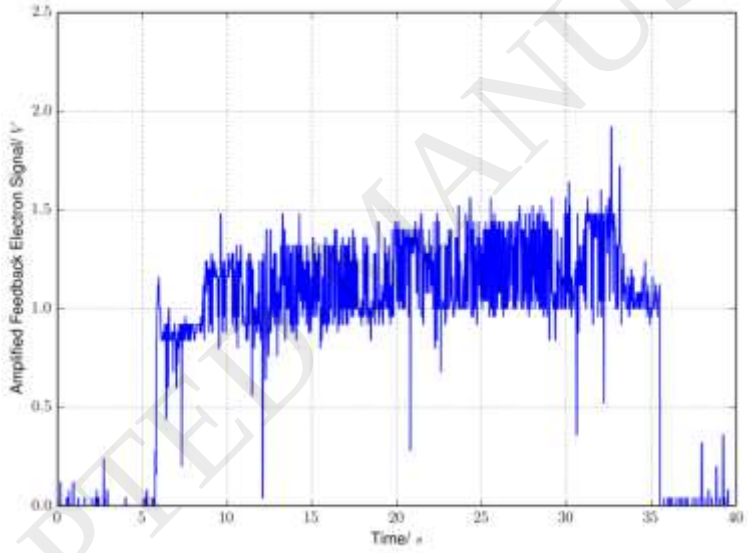

(c)

Fig. 13. (a) Imaging area of $180mm \times 180mm$ $(W \times D)$ and typical examples of the corresponding subsystem signals: (b) processed machine X scan signal plotted alongside the scan line synchronisation signal generated by the data logger and (c) amplified feedback electron signals

Fig. 13 (b) and **(c)** show the signals recorded when the primary electron beam was raster-scanning a $180mm \times 180mm$ $(W \times D)$ area shown in **Fig. 13 (a). Fig. 13 (b)** demonstrates that the prototype picked up the start of each sawtooth waveform, which is the condition machine X scan signals, by switching the X scan line synchronisation signal from logic LOW to logic HIGH. **Fig. 13(c)** gives a set of amplified feedback electron signal from one image frame. The feedback electron signal was obtained from the interactions between the EBM machine primary electron beam and the surface of the standard electronic imaging test build. Digital images were generated from the image generation software by suitably collating the feedback electron signal with the processed EBM machine X scan signal.

Image processing was carried out on the raw digital images generated from the electronic imaging trials. Image noise was removed by applying a median filter and image contrast was enhanced by carrying out histogram equalisation. **Eq. 2** (Gonzalez et al, 2008) and **Eq. 3** (Gonzalez et al., 2008) define the median filter and histogram equalisation functions used respectively.

$$\hat{f}(x,y) = \underset{(s,t)\in S_{xy}}{median}\{g(s,t)\} \tag{2}$$

Where

$\hat{f}$ (x,y) is the pixel-value of the filtered image at (x,y)

g(s,t) is the pixel-value of the raw image at (s,t)

S_{xy} represents the set of coordinates within a user-defined area of the image

$$y_k \triangleq \left\lfloor \left[(L-1)\sum_{i=0}^{k} h(i) \right] + 0.5 \right\rfloor \qquad k = 0, 1, 2, \ldots\ldots, L-1 \tag{3}$$

Where

L is the bit depth of an image

k is the pixel value within the bit depth

h(i) is the normalised histogram which gives the probability of occurrence of pixel value i

$\sum_{i=0}^{k} h(i)$ is the cumulative probability distribution of the normalised histogram

y_k is an integer, the equalised number of pixel at pixel value k

Fig. 14 (a) shows a typical raw digital image generated from the electronic imaging system prototype during the imaging trials. **Fig. 14 (c)** and **(e)** are processed images with noise removed and image contrast enhanced. **Fig. 14 (b)**, **(d)** and **(f)** are the histograms of the above three images.

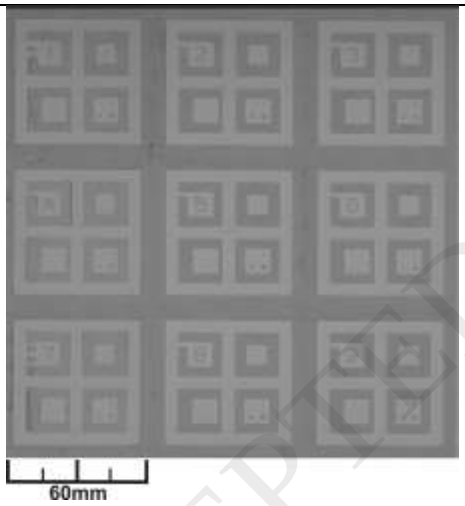

(a)

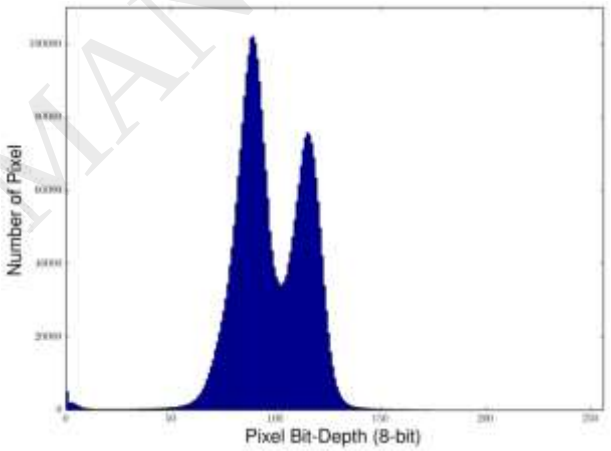

(b)

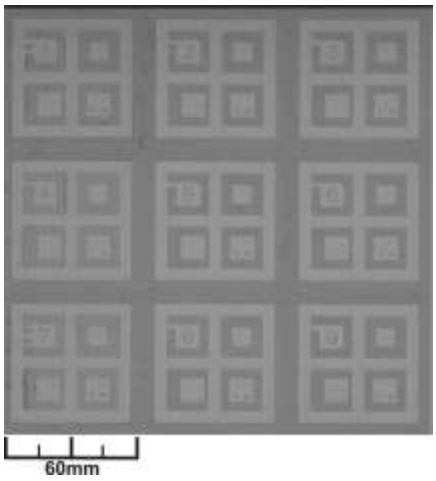

(c)

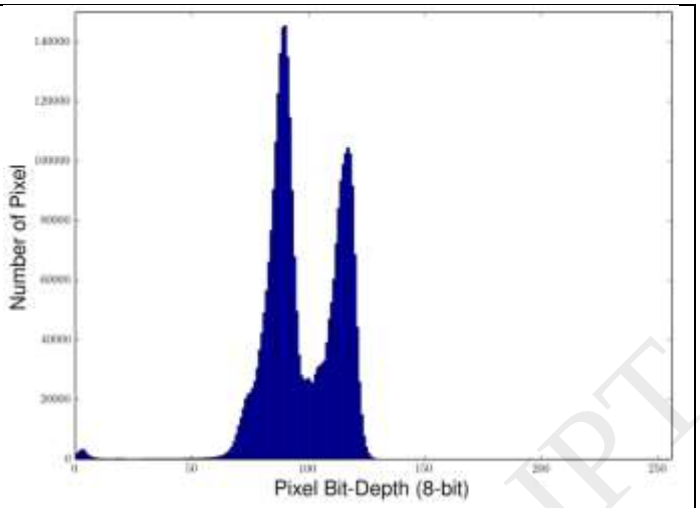

(d)

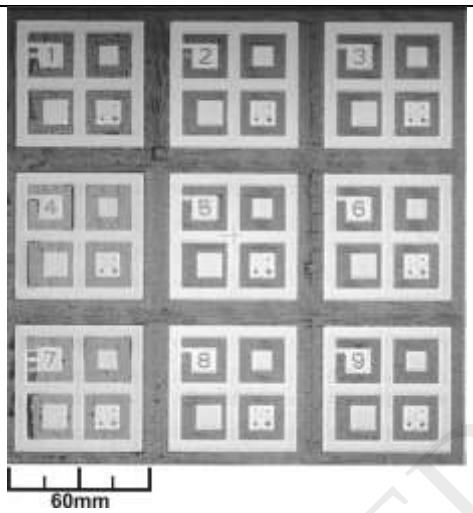

(e)

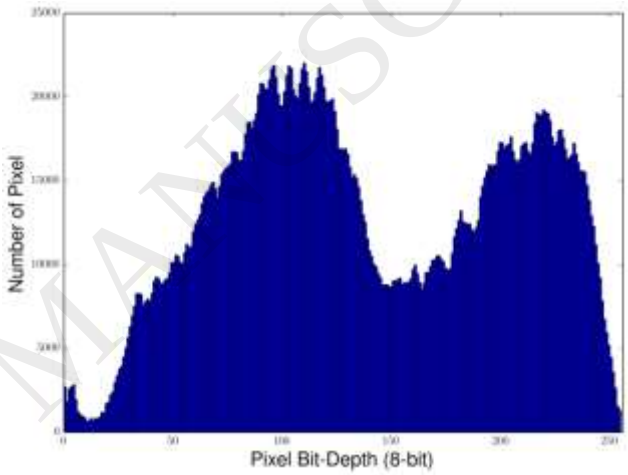

(f)

Fig. 14 (a). An 8-bit, 1800 $pixel$ × 1800 $pixel$ (row × $column$) digital electronic image (raw) covering an imaging area of 180mm × 180mm (W × D) in the EBM machine processing area generated at room temperature and (b) its histogram. (c) The image with median filter applied for noise removal and (d) its histogram. (e) The further processed image with histogram equalisation applied for contrast enhancement and (f) its histogram.

Digital Image Generation at Elevated Temperatures

In the third set of experiment, the Ti-6Al-4V test build was heated up by the machine electron beam and single-layer electronic imaging trials were carried out under elevated temperature. **Fig. 15** shows the temperature profile during experiment. The temperature of the test build ramps up from room temperature, plateaus around $200°C$ for approximately 10 minutes, before rising again until around $320°C$. The stagnation around $200°C$ was due to multiple faults on the machine electron beam. When the electron beam raster-scanned the test build during heating, some positively charged metal vapour or loosely-bound particles from the test build surface accelerated towards the electron gun cathode and anode, which were held at negative electric potentials relative to the grounded test build, leading to high-voltage vacuum breakdown via arc-discharge between the cathode and the anode (Maiti et al, 2014). Multiple arcing warnings were flagged up by the EBM machine computer and the machine took around 10 minutes to stabilise. Electronic imaging experiment was eventually carried out after heating resumed and the test build temperature reaching approximately $320°C$.

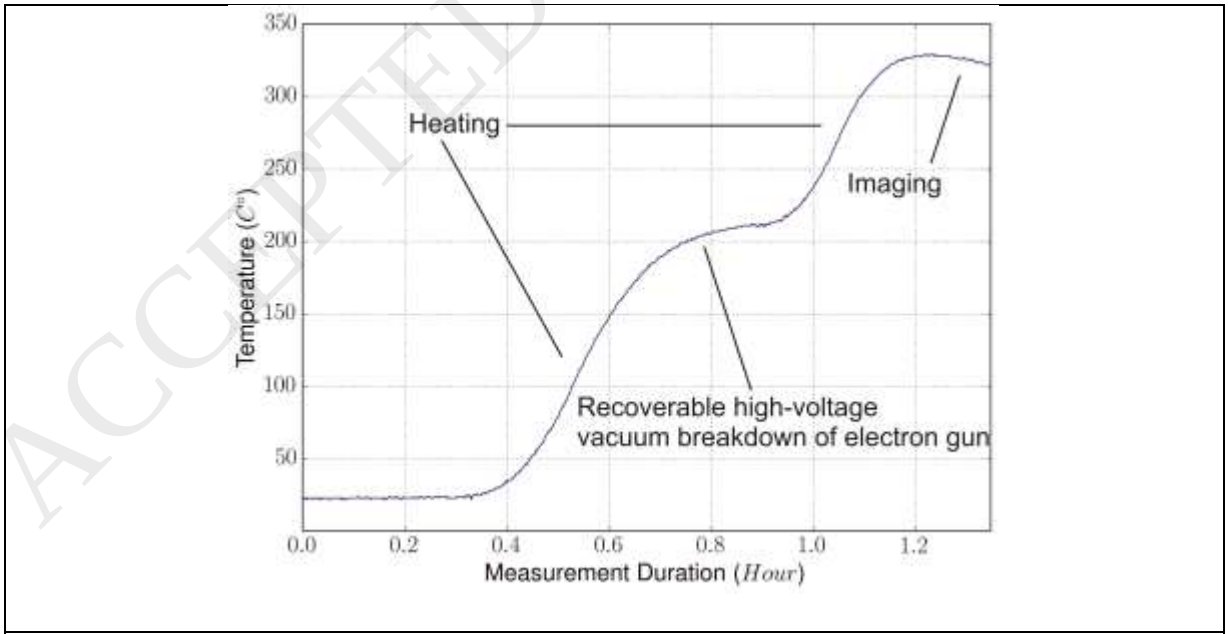

Fig. 15. Temperature profile of the Ti-6Al-4V test build during electronic imaging experiment at elevated temperature

Fig. 16 (a) is a screenshot taken from the EBM machine computer, showing an image captured by the machine near-IR camera when the test build temperature was at approximately $320°C$. The image was captured when the machine chamber light was turned off. A bright circular spot in the centre of the test build can be observed. **Fig. 16 (b)** is a screenshot which shows an imaged captured when the machine chamber light was turned on.

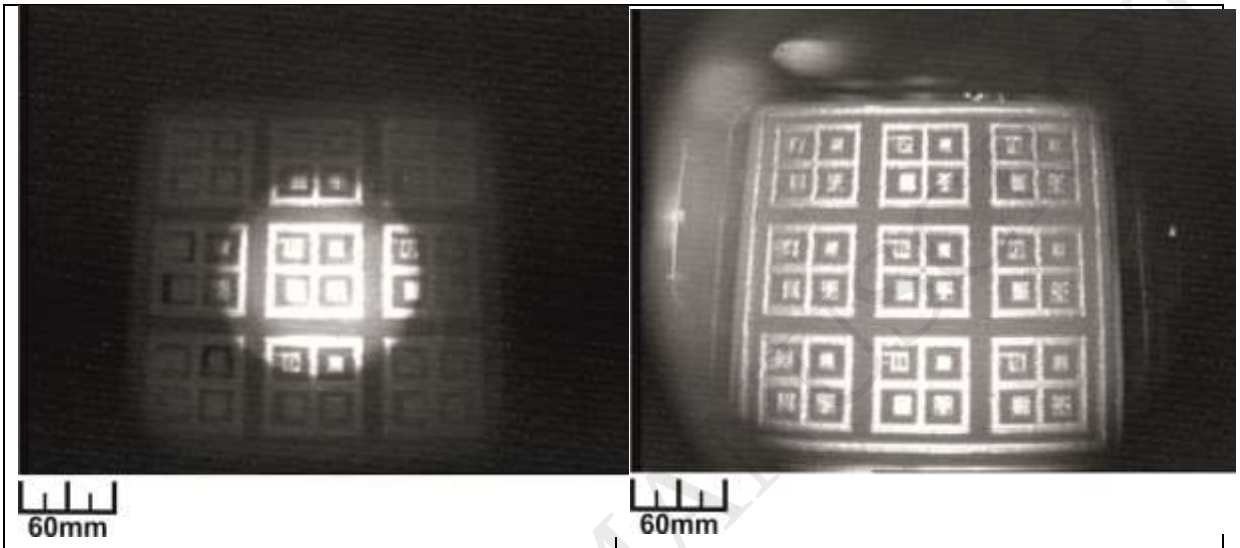

(a) (b)

Fig. 16. EBM machine computer screenshots of images taken from the machine near-IR camera at approximately $320°C$, on the Ti-6Al-4V test build (a) with machine chamber light turned off and (b) turned on.

Fig. 17 (a)-(d) show typical raw and processed electronic images and their histograms. **Fig. 17(a)** is the raw image generated when the test build was at approximately $320°C$. **Fig. 17(c)** is the processed image with noise filtered and contrast enhanced, in accordance with the methods described by **Eq. 2** and **3**. **Fig. 17 (b)** and **(d)** are the histograms of the described raw and processed images.

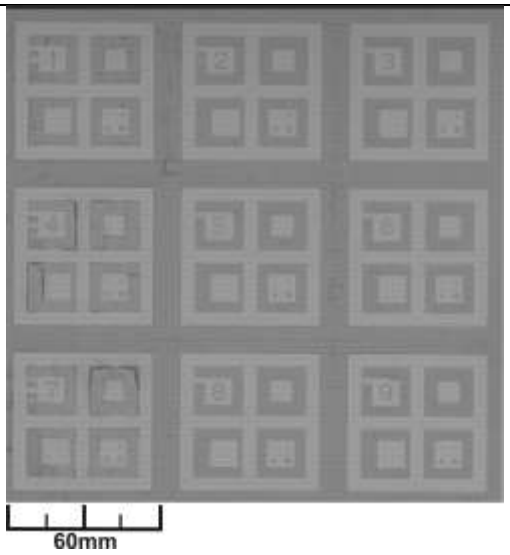

(a)

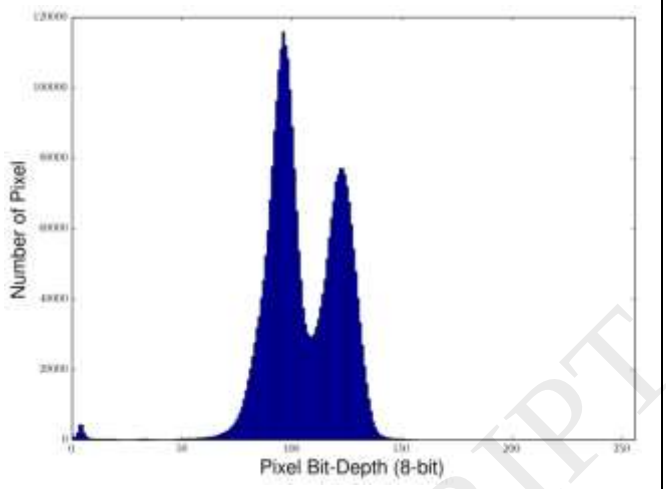

(b)

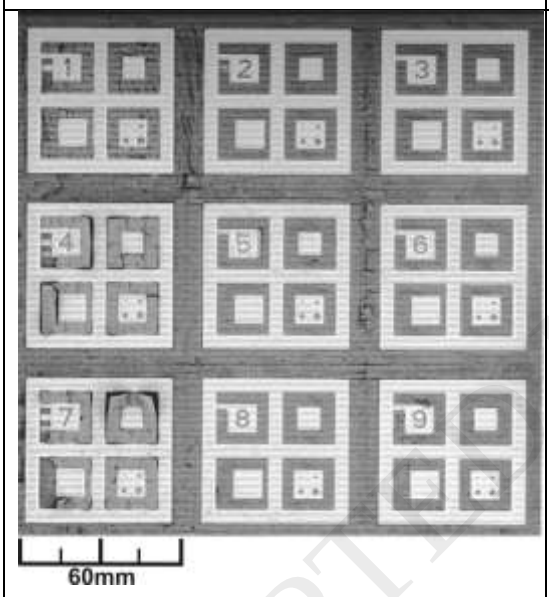

(c)

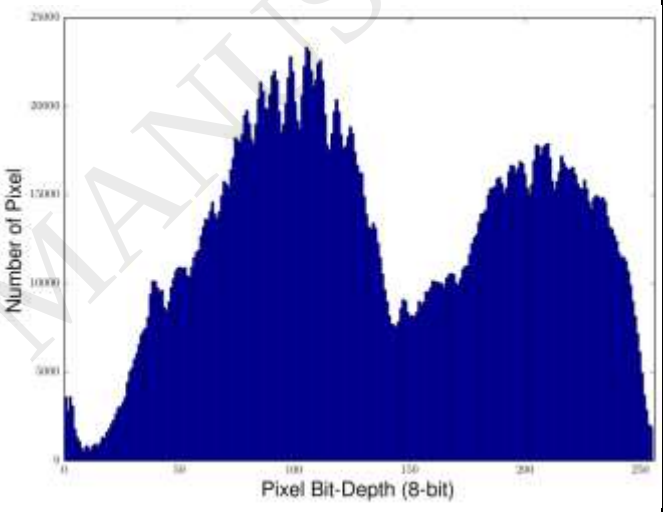

(d)

Fig. 17 (a). An 8-bit, 1800 $pixel$ × 1800 $pixel$ (row × $column$) digital electronic image (raw) covering an imaging area of 180mm × 180mm (W × D) in the EBM machine processing area generated at approximately 320°C and (b) its histogram. (c) The processed image with median filter applied for noise removal and histogram equalised for contrast enhancement and (d) its histogram

Fig. 18 is an image taken after the experiment. It demonstrates the damage done to the test build surface during heating. The figure shows horizontal surface markings and delamination around the $60mm \times 60mm$ imaging location 7.

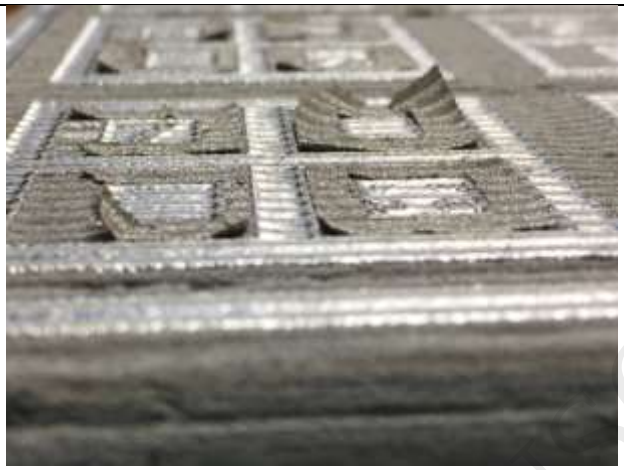

Fig. 18. An optical image taken after experiment, showing delamination of the test build surface and horizontal markings around imaging location 7

Histogram quality analyses were carried out on both the raw and processed digital electronic images generated at room temperature and approximately $320°C$. **Reiter et al (2014)** describe an image quality measure Q in their studies on histogram-based images. **Eq. 4** and **Fig. 19** give the definition of the quality measure Q.

$$Q = \frac{|\mu_2 - \mu_1|}{\sqrt{\sigma_1^2 + \sigma_2^2}} \quad (4)$$

Where

Q is the image quality measure

μ_i is the within-class mean, $i = 1, 2$, the pixel value class present

σ_i is the within-class standard deviation, $i = 1, 2$, the pixel value class present

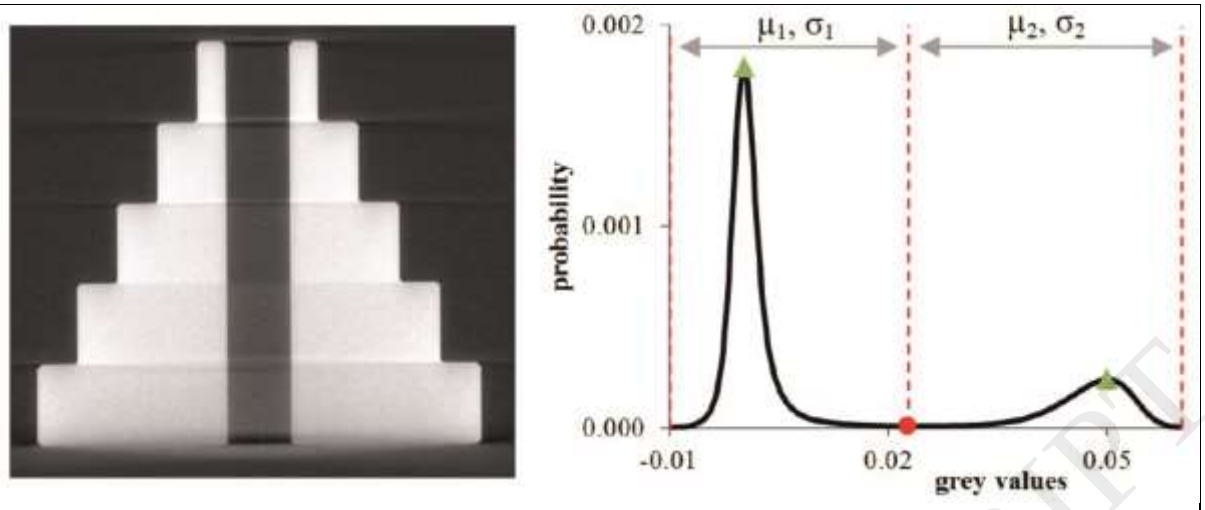

Fig. 19. A demonstration image and its bimodal histogram showing the definitions of threshold, within-class mean and within-class standard deviation (Reiter et al, 2014)

This image quality measure Q represents the degree of separation between the two pixel value classes in the histogram of interest. An image of ideal quality is defined as to consist of minimum noise and blur. The separation of the classes in its histogram is maximised while the classes' within-class standard deviations minimized. Thus the greater the Q value, the better the image quality. As this measure Q takes into account noise and blur, it gives a global impression on image quality. The four histograms obtained from experiments, as described in **Table. 6**, went through Otsu thresholding (Otsu, 1979) for the estimation of their pixel value classification thresholds. Thresholding was then followed by image quality measure Q analyses of the histograms. Results are summarised in **Table. 7**. **Fig. 16 (a)** and **(b)** are thermal images taken by the EBM machine near-IR camera at approximately $320°C$. They were excluded from the histogram quality analysis as they contained either an undesired bright spot or an ill-defined ROI when compared with their digital electronic image counterparts. These factors affect the analysis accuracy.

Table. 6. The four histograms involved in image quality measure Q analyses

Histogram Name	Temperature	Image Condition	Figure
RT_Raw	Room temperature	Raw	14 (b)
RT_Processed	Room temperature	Processed	14 (f)
320_Raw	$320°C$	Raw	17 (b)
320_Processed	$320°C$	Processed	17 (d)

Table. 7. Histogram quality measure Q analyses. Data are rounded to 3.s.f.

Histogram	Threshold	μ_1	μ_2	σ_1	σ_2	Q	ΔQ	$\Delta Q / Q_{min}$
RT_Raw	99.0	84.8	113	11.8	7.95	2.02	0.05	2.48%
320_Raw	107	92.8	121	11.8	7.18	2.07		
RT_Processed	147	90.9	203	32.2	27.5	2.65	0.02	0.75%
320_Processed	145	88.8	201	31.4	28.0	2.67		

Discussion

Discussions on the results are presented in this section. Observations in system prototype capability verification and digital electronic image generation at both room and elevated temperatures are analysed and explained.

System Capability Verifications

The benchtop test was conducted to verify the digital image generation capability of the prototype. 800 $pixel$ × 2000 $pixel$ (row × $column$) digital images (**Fig. 12 (a)**) were generated by the image generation software via waveform reconstruction from the two virtual

electrical signals. In addition, results from the analysis of 60,000 virtual feedback electron signal data points show that, both C_V and μ of the pixel value data set for each of the three-stripe regions are less than 3% different from their theoretical values (**Table. 4**). This indicates that the data logger can sample the virtual feedback electron signal and reproduces the three colours of the reconstructed image with the above mentioned accuracy. Moreover, **Fig. 12(b)** and **Table. 5** show that no variations are found in the number of pixels in any of the three-stripe regions over 30 reconstructed waveforms, when compared with their theoretical values. These results suggest that the data acquisition of the virtual feedback electron signal is synchronised with the generation of the virtual machine X scan signal and thus, results in a reconstructed image with three equally spaced stripes.

It is thought that the electronic imaging system prototype capability has been verified by the reconstruction of the three-stripe image with adequate sampling accuracies in both time and logged values.

Digital Image Generation at Room Temperature

The electronic imaging trails were conducted to explore the possibility of EBM in-process monitoring via electronic imaging. Prototype subsystem electrical signals were monitored during the imaging trials for potential trouble shooting purposes. The system showed that it could generate scan line synchronisation signal and amplified feedback electronic signal for the generation of digital images. In **Fig. 13 (b)**, the conditioned machine X scan signal is plotted alongside the scan line synchronisation signal. The rising edges of the synchronisation signal are aligned with the start of the X scan signal sawtooth waveforms. As the generation of a digital electronic image involved the allocation of individual pixel value, which is converted from the obtained feedback electron signal, synchronisation between data acquisition and the movement of the primary electron beam is critical. The generation of the

synchronisation signal confirmed that the prototype can conduct data acquisition according to the beam movement. **Fig. 13 (c)** shows the amplified feedback electron signal. Raw feedback electron signal was processed and configured to be within the prototype input range of $0V$ to $+3.3V$.

Digital electronic images were generated during imaging trials. The typical raw image generated (**Fig. 14 (a)**) achieves the correct user-defined size and bit depth. Image contrast is observed between regions of solidified Ti-6Al-4Vsurface and sintered Ti-6Al-4V powder. **Fig. 14 (b)** is the histogram of the raw image and it shows two pixel value peaks. The peaks correspond to the regions of solidified surface and sintered powder respectively. **Reig et al. (2013)** investigated the bulk porosity of sintered Ti-6Al-4V powder and reported that the porosity is approximately 32% for powder of $180\mu m - 600\mu m$ in size, after being sintered at $1300°C$ to $1400°C$ for up to eight hours. It is thought that the darker colour (lower in pixel value) regions in **Fig. 14 (a)** come from the bulk porosity of the sintered powder. From a qualitative perspective, it is believed that there is less material to interact with the primary electron beam for a given area in the sintered powder when compared with that of the solidified surface. This leads to a lower feedback electron signal level and thus a lower pixel value.

A median filter was applied to raw images in order to reduce noise. The typical noise-filtered image (**Fig. 14 (c)**) has a histogram (**Fig. 14 (d)**) with two peaks, in which the numbers of pixels are higher than those in the raw image histogram (**Fig. 14 (b)**), as expected after noise removal (approximately 140000 and 100000 pixels in **Fig. 14 (d)** against approximately 100000 and 80000 pixels in **Fig. 14 (b)**). The median filter functions by replacing the target pixel value with the median pixel values of a user-defined neighbourhood surrounding the target pixel. Consequently, pixels containing noise, i.e. pixels values with large differences when compared with that of the neighbourhood, are replaced by the median

pixel values of the neighbouring pixels. This leads to more pixels falling into the two main pixel value groups which manifest themselves as two higher peaks in **Fig. 14 (d**).

Noise removal was followed by histogram equalisation. The typical resultant image (**Fig. 14 (e)**) has a histogram (**Fig. 14 (f)**) in which the pixel values are more spread out and occupy the whole available bit depth, when compared with **Fig. 14 (d)**. Consequently, **Fig. 14 (e)** presents the test build features with greater contrast to the background when compared with **Fig. 14 (a)** and **(c).**

The digital electronic images successfully show the nine imaging locations across the machine processing area, and demonstrate image contrast between solidified Ti-6Al-4Vsurface and sintered Ti-6Al-4V powder.

Digital Image Generation at Elevated Temperature

Fig. 15 shows the test build temperature profile measured. Electronic imaging trials were carried out at approximately $320°C$. A negative heating rate is observed from **Fig. 15** at 1.2 hours into the experiment. This suggests that the test build struggled to maintain its temperature during the experiment. It is thought that the current in-house developed heating scan strategy failed to raise the test build temperature beyond $320°C$ via electron beam heating, due to heat loss to the machine chamber. Electron beam heating pattern and parameters different from those used in the experiment (**Fig. 5(b)** and **Table. 3**) will be explored in future studies to improve heating efficiency.

Fig. 16 (a) and **(b)** are EBM machine computer screenshots of images taken by the machine near-IR camera at approximately $320°C$. The bright spot in **Fig. 16 (a)** is thought to be attributed to incandescence of the electron gun cathode. The EBM machine has a thermionic electron gun (Wysocki et al, 2017), when the tungsten cathode gets heated, it emits blackbody radiation according to Planck's law (Jain et al, 1998). When the machine

chamber light was turned on during experiment, the image contrast due to incandescence was no longer observable, as demonstrated by **Fig. 16(b)**. The effect of cathode incandescence is thought to be a potential issue with thermal / optical imaging systems. These systems rely on the correct operation of the machine chamber light. If the chamber light malfunctions, the quality of the images captured during in-process data collection would be compromised.

Fig. 17 (a) shows a typical, raw digital electron image generated at approximately $320°C$. In comparison to **Fig. 16(a)** and **(b),** the image FOV of **Fig. 17(a)** only consists of an user-defined 180 mm ×180 mm (W×D) Regions of Interest (ROI), without including any monitoring-irrelevant regions beyond the machine processing area. Thus, all image pixels are carrying useful information for monitoring. In addition, the electronic imaging mechanism guarantees the generation of an orthogonal projection of the ROI. Therefore, the digital electronic images do not suffer from the keystone distortion (distortion of geometry due to non-orthogonal projection) as observed in **Fig. 1(b)** and **Fig. 16(b)**. In addition, **Fig. 14(a)** and **Fig. 17(a)** are raw electronic images generated when the chamber light was switched off. They show that cathode incandescence does not influence the electronic image quality. It is because whilst energy of the electron cathode blackbody radiation is carried by photons, the electron sensor in the prototype only registers electrons impinging onto its sensing surface. The blackbody radiation is invisible to the electronic imaging system. Moreover, when compared with the EBM machine near-IR image of **Fig. 16(b)**, even the raw electronic image of **Fig. 17(a)** reveals more topographical details of the test build. **Fig. 17(a)** shows that all imaging location numbers are identifiable and damages on the test build due to heating can be observed. The horizontal markings across the whole image, cracks in the sintered powder areas and delamination around imaging location 4 and 7 are thought to be damages due to heating of the test build. **Fig. 18** is an optical image taken after the imaging experiment,

which gives a zoomed-in perspective onto imaging location 7. The figure confirms that there is delamination around imaging location 7.

It is thought that the digital electronic image quality is temperature independent, between room temperature and approximately $320°C$. Histogram quality analyses were carried out on four electronic images and global image quality measure Q values were calculated. **Table. 7** shows that the difference in Q values between raw electronic images taken at room temperature and at approximately $320°C$ is less than 3%. The difference in Q values drops to below 1% when the images are processed in accordance with **Eq. 2** and **3** (noise filtered and contrast enhanced). The temperature range will be extended in future studies to include the in-process monitoring temperature, i.e. approximately $700°C$ for Ti-6Al-4V (demonstrator material), in order to give a bigger picture of the influence of temperature on image quality.

Conclusions

An electronic imaging system prototype has been presented in this paper. Although the prototype was designed only for the Arcam A1 EBM machine in this study, it is thought that the design process and technical details described can serve as references to readers who wish to carry out similar work on other EBM machines.

Capability of the prototype was verified by both benchtop simulations and by interfacing with a commercial EBM machine. With the use of the prototype, single-layer electronic imaging trials were carried out on a standard electronic imaging test build in the EBM machine at both room temperature and approximately $320°C$, and digital electronic images were generated. Comparisons between near-IR and electronic images were made. It is observed that the electronic image FOV is confined to the user-defined ROI and the electronic images are not keystone distorted. Moreover, electronic images are not affected by

electron gun cathode incandescence. In addition, image contrast between sintered Ti-6Al-4V powder and its solidified surface is observed. Comparisons between electronic images generated at room temperature and approximately $320°C$ were made. It is observed that the difference in histogram quality measure Q values is less than 3% for the comparison between raw electronic images and less than 1% for that between processed electronic images. Electronic image quality has been shown to be almost independent of temperature within the temperature range involved in this study.

With regard to in-process EBM data collection, it is thought that the electronic imaging system prototype has the potential to be an alternative to systems which employ thermal or optical imaging. There will be challenges moving to in-process data collection in order to realise the potential. They are thought to include, carrying out imaging on multi-layer for the whole additive manufacturing process, working at in-process, elevated temperature as the EBM cycle includes preheating of the processing area and dealing with metallisation generated from vaporisation of metal powder during the EBM process. With realisation of the described development, it is envisaged that data analysis with machine learning techniques could be conducted on the collected data for defect detection purposes. The combination of data collection and data analysis will enable an in-process EBM monitoring system to be developed. An EBM monitoring system in turn is thought to be crucial for research on feedback defect-corrective actions. This chain of future development will eventually lead to a close-loop control EBM machine, enabling the effective manufacture of certified metal components for safety-critical industries, including medical device, aerospace, automotive, and nuclear industry.

Acknowledgements

The Author(s) declare(s) that there is no conflict of interest. This research received no specific grant from any funding agency in the public, commercial, or not-for-profit sectors. The machine was purchase, in part from a grant received for the EPSRC Centre for Innovative Manufacturing in Additive Manufacturing.

References

Gibson, I., Rosen, D.W., Stucker, B., 2010. Additive Manufacturing Technologies. Springer, New York

Gong, X., Anderson, T., Chou, K., 2014. Review on Powder-Based Electron beam Additive Manufacturing Technology. Manufacturing Review 1 2. DOI: 10.1051/mfreview/2014001

Harrysson, O.L.A, Cansizoglu, O., Marcellin-Little, D.J., Cormier, D.R., West, H.A., 2008. Direct metal fabrication of titanium implants with tailored materials and mechanical properties using electron beam melting technology, Materials Science and Engineering: C, Volume 28, Issue 3, 2008, Pages 366-373, ISSN 0928-4931, http://dx.doi.org/10.1016/j.msec.2007.04.022.

Baudana, G., Biamino, S., Ugues, D., Lombardi, M., Fino, P., Pavese, M, Badini, C., 2016. Titanium aluminides for aerospace and automotive applications processed by Electron Beam Melting: Contribution of Politecnico di Torino, Metal Powder Report, Volume 71, Issue 3, 2016, Pages 193-199, ISSN 0026-0657, http://dx.doi.org/10.1016/j.mprp.2016.02.058.

Jarow, J.P., Baxley, J.H., 2015. Medical devices: US medical device regulation, Urologic Oncology: Seminars and Original Investigations, Volume 33, Issue 3, March 2015, Pages 128-132, ISSN 1078-1439, https://doi.org/10.1016/j.urolonc.2014.10.004.

Portolés, L., Jordá, O., Jordá, L., Uriondo, A., Esperon-Miguez, M., Perinpanayagam, S., 2016. A qualification procedure to manufacture and repair aerospace parts with electron beam melting, Journal of Manufacturing Systems, Volume 41, 2016, Pages 65-75, ISSN 0278-6125, http://dx.doi.org/10.1016/j.jmsy.2016.07.002.

Mani, M., Lane, B., Donmez, A., Feng, S., Moylan, S., Fesperman, R., 2015. NISTIR 8036 Measurement Science Needs for Real-time Control of Additive Manufacturing Powder Bed Fusion Processes. http://dx.doi.org/10.6028/NIST.IR.8036

Scharowsky, T., Bauereiß, A., Singer, R.F., Körner, C., 2012. Observation and numerical simulation of melt pool dynamic and beam powder interaction during selective electron beam melting. Proceedings from the Solid Freeform Fabrication Symposium, Austin, pp 815–820

Price, S.,Cooper, K., Chou, K., 2012. Evaluations of Temperature Measurmnets by Near-Infrared Thermography in Powder-Based Electron-Beam Additive Manufacturing. Proceedings from the Solid Freeform Fabrication Symposium, pp. 761-773

Dinwiddie, R.B., Dehoff, R.R, Lloyd, P.D., Lowe, L.E., Ulrich, JU.B.,2013. Thermographic In-Situ Process Monitoring of the Electron-Beam Melting Technology Used in Additive Manufacturing. Proc. SPIE 8705, Thermosense: Thermal Infrared Applications XXXV, 87050K; doi:10.1117/12.2018412

Schwerdtfeger, J., Singer, R.F., Körner, C., 2012. In situ flaw detection by IR-imaging during electron beam melting, Rapid Prototyping Journal, Vol. 18 Issue: 4, pp.259-263, https://doi.org/10.1108/13552541211231572

Rodriguez, E., Medina, F., Espalin, D., Terrazas, C., Muse, D., Henry, C., MacDonald, E., Wicker, R., 2012. Integration of a thermal imaging feedback control system in Electron Beam Melting. Proceedings from the Solid Freeform Fabrication Symposium, pp 945–961

Mireles, J., Terrazas, C., Gaytan, S.M., Roberson, D.A., Wicker, R.B., 2015. Closed-Loop Automatic Feedback Control in Electron Beam Melting, Int J Adv Manuf Technol. 78: 1193. doi:10.1007/s00170-014-6708-4

Watt, I.M., 1997. The Principles and Practice of Electron Microscopy, Cambridge University Press, pp. 90-95. Book DOI: http://dx.doi.org/10.1017/CBO9781139170529

Reimer, L., 1998. Scanning Electron Microscopy: Physics of Image Formation and Microanalysis, Springer, pp. 3-4, 135-165

Oatley, C.W., 1972. The Scanning Electron Microscope: Part I The Instrument, Cambridge University Press, pp. 1-2, 134-165

Postek, M.T., Vladár, A.E., 1996. Digital Imaging for Scanning Electron Microscopy, Scanning. Volume 18, 1-7. DOI: http://dx.doi.org/10.1002/sca.1996.4950180101

Egerton, R.F., 2005. Physical Principles of Electron Microscopy, Springer, pp. 137 –139

Dutta, B., Froes, F.H., 2017. The Additive Manufacturing (AM) of titanium alloys, Metal Powder Report, Volume 72, Issue 2, Pages 96-106, ISSN 0026-0657, https://doi.org/10.1016/j.mprp.2016.12.062

Kirchner, A., Klöden, B., Luft, L., Weißgärber, T., Kieback, B., 2014. Process Window for Electron Beam Melting of Ti-6Al-4V, Proceeding of EuroPM 2014 – AM Technologies

Gonzalez, R.C., Woods, R.E., 2008. Digital Image Processing, Pearson Eductaion, Inc., pp. 122-127, 322-327

Maiti, N., Thakur, K.B., Patil, D.S., Das, A.K., 2014. High voltage breakdown studies in electron gun and its damage control, International Symposium on Discharges and Electrical Insulation in Vacuum (ISDEIV), Mumbai, pp. 37-39, doi: 10.1109/DEIV.2014.6961613

Reiter, M., Weiss, D., Gusenbauer, C., Erler, M., Kuhn, C., Kasperl, S., Kastner, J., 2014. Evaluation of a Histogram-Based Image Quality Measure for X-ray Computed Tomography, Proceedsing of Conference on Industrial Computed Tomography 2014

Otsu, N., 1979. A Threshold Selection Method from Gray-Level Histograms, IEEE Transactions on Systems, Man, and Cybernetics, Vol. SMC-9, No.1

Reig, L., Tojal, C., Busquets, D., Amigó, V., 2013. Microstructure and Mechanical Behavior of Porous Ti-6Al-4V Processed by Spherical Powder Sintering, Materials, Vol. 6 Issue:10, pp. 4868-4878, doi:10.3390/ma6104868

Wysocki, B., Maj, P., Sitek, R., Buhagiar, J., Kurzydłowski, K.J., Święszkowski, W., 2017. Laser and Electron Beam Additive Manufacturing Methods of Fabricating Titanium Bone Implants. Applied Sciences. 2017; 7(7):657. https://doi.org/10.3390/app7070657

Jain, P.K., Sharma, L.K., 1998. The Physics of blackbody radiation: A review , Journal of Applied Science in Southern Africa 4(2):80-101, DOI: 10.4314/jassa.v4i2.16899